

Time- and frequency-resolved detection of atomic coherence in the regime of strong-field interaction with intense femtosecond laser pulses

S. O. Konorov,^{1,2} J. W. Hepburn,^{1,2,3} and V. Milner^{1,2,3}

¹*Department of Chemistry, The University of British Columbia, Vancouver, British Columbia, Canada*

²*The Laboratory for Advanced Spectroscopy and Imaging Research (LASIR), The University of British Columbia, Vancouver, British Columbia, Canada*

³*The Department of Physics & Astronomy, The University of British Columbia, Vancouver, British Columbia, Canada*

(Received 16 November 2010; published 24 March 2011)

Understanding the effect of strong laser pulses on the evolution of an atomic or molecular wave function is important in the context of coherent control in the strong-field regime, when power broadening and dynamic Stark shifts become comparable with or bigger than the bandwidth of the control field. We experimentally demonstrate the method of complete characterization of a complex-valued amplitude of a quantum state driven by a strong two-photon field. The method is based on coherent scattering of a weak probe pulse from the strong-field-induced atomic coherence, followed by the detection of the time- and frequency-resolved parametric four-wave-mixing signal. We show that the proposed technique corresponds to a cross-correlation frequency-resolved optical gating (XFROG) of the highly perturbed evolution of an atomic quantum state. Utilizing the XFROG retrieval algorithm, we determine both the amplitude and phase of an atomic wave function at any time moment throughout the interaction with the driving field. The direct retrieval of the time-dependent phase of the wave function, rather than the population dynamics only, enables us to observe the strong-field effects with arbitrary time and frequency resolution.

DOI: [10.1103/PhysRevA.83.033417](https://doi.org/10.1103/PhysRevA.83.033417)

PACS number(s): 32.80.Qk, 42.50.Ct

I. INTRODUCTION

Constantly increasing pulse energies from readily available ultrafast laser sources resulted in a growing volume of work on strong-field control of the interaction of atoms and molecules with intense laser fields. High-power ultrashort laser pulses have become a common tool in driving highly nonlinear, and therefore typically inefficient, optical processes from two-photon absorption to four-wave mixing (FWM) to multiphoton ionization and high-harmonic generation. Although the amplitude of a signal of interest can be dramatically increased by increasing the field strength, the latter is usually accompanied by a series of undesired strong-field effects, such as energy ladder climbing [1] and dynamic Stark shifts (DSSs) [2].

DSSs could be particularly harmful to spectroscopic measurements as the notion of tuning the laser “on resonance” breaks down due to the time-dependent frequency shifts of strongly driven atomic or molecular resonances. Similarly, multiple schemes of coherent control rely on controlling interferences between resonant and nonresonant quantum pathways [3,4], and hence on a static rather than dynamically changing energy spectrum of the system. Unlike the strong-field effects on a single-photon resonance, e.g., Autler-Townes splitting [5] and Rabi oscillations [6], multiphoton transitions are harder to control due to the increasing number of interfering on- and off-resonant interaction channels [7]. The latter cannot be neglected as they are the essential intermediate steps toward the final target state. A number of routes to multiphoton strong-field coherent control, in which DSSs have been either avoided or compensated for, have been proposed and implemented. These include the use of chirped pulses [8–10], pulse trains [11,12], “real fields” [13], spectral phase jumps [14,15], and adaptive atom-field phase matching [16,17].

Typical strong-field control schemes aim at the enhancement or suppression of the population transfer from the initial

to the target quantum state [17], a superposition of states [18], a continuum of states [19], or even a dressed state [9,11]. At the same time, the efficiency of the population transfer is governed by the dynamically changing phases of, and therefore coherences between, the Stark shifted atomic states. Hence, the detection of the target state population offers only an incomplete picture of the dynamics of a strongly driven system. For a full understanding of these dynamics, one needs to be able to detect and analyze the time-dependent laser-induced coherences. Here, we demonstrate a method of measuring strong-field-induced coherences and show a robust way of analyzing them in both frequency and time domains, with a resolution not limited by the spectral bandwidth of the excitation pulses or their duration, respectively. The evolution of atomic coherences in time and frequency reflects the effects of the strong-field excitation, e.g., the dynamic splitting and shifting of resonances in response to the time-dependent driving field.

Studying laser-induced coherences under strong-field excitation is also motivated by nonlinear spectroscopy, e.g., coherent anti-Stokes Raman scattering, where enhancing the nonlinear response of the medium is often achieved by increasing the strength of the excitation fields beyond the perturbative limit [20]. As shown in this work, dynamic Stark shifts modify the spectrum of coherently scattered photons, prohibiting accurate measurements of the resonant frequencies. The ability to measure transient behavior, i.e., the evolution of the molecular quantum state *during* the interaction with the strong driving field is also important in the context of strong-field coherent control, when intermediately populated quantum states could be coupled to irreversible decay channels, such as photoionization or dissociation.

This paper is organized as follows. In Sec. II, we describe the details of the method and present the results of numerical simulations of the proposed experimental detection technique.

Section III outlines the details and results of our experimental measurements. In order to analyze the experimental results, we first work out an analytical model of the atomic response, presented in Sec. IV. The theoretical analysis enables us to apply the technique of cross-correlation frequency-resolved optical gating for interpreting the experimental observations in Sec. V, which is followed by a brief summary.

II. NUMERICAL CALCULATIONS

To measure both the amplitude and phase of the complex-valued coherences, we use a *parametric* four-wave mixing process in atomic rubidium, depicted in Fig. 1. The scheme is different from the previously studied superfluorescence in a double-cascade configuration, in which the emission is stimulated by a field resonant with an atomic transition [21,22]. In our case, two strong pump fields $E_1(t)$ and $E_2(t)$ of frequencies ω_1 and ω_2 move the atomic population and induce coherence between the ground level $|1\rangle \equiv |5s\rangle$ and excited level $|3\rangle \equiv |4d\rangle$ of Rb. An intermediate state $|2\rangle \equiv |5p\rangle$ is not covered by the spectral bandwidth of the excitation pump pulses, but its close proximity to a single-photon resonance

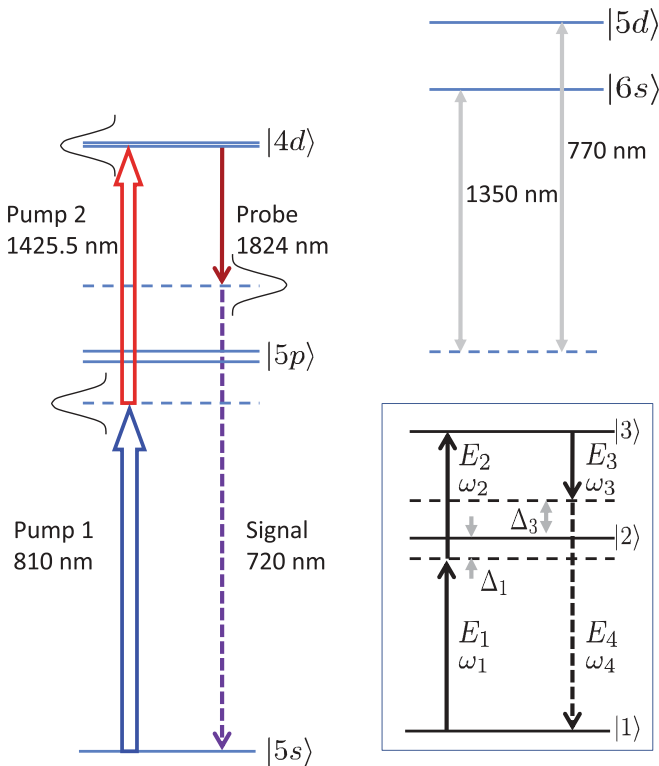


FIG. 1. (Color online) Parametric four-wave-mixing process in atomic rubidium used in this work. Two strong pump fields, pump 1 and pump 2 (wide vertical arrows), move the atomic population and induce coherence between the ground level $|1\rangle \equiv |5s\rangle$ and excited level $|3\rangle \equiv |4d\rangle$ of Rb. The latter is detected by scattering a weak off-resonant probe pulse (solid narrow arrow) and detecting the FWM signal (dashed narrow arrow). Hyperfine splitting of $|5p\rangle$ and $|4d\rangle$, as well as two other electronic states $|6s\rangle$ and $|5d\rangle$, shown in the upper right corner, were taken into account in the numerical calculations described in Sec. II. The inset shows a simplified three-level model used in the theoretical analysis of Sec. IV.

introduces significant Stark shifts of the two states coupled by a two-photon resonance, affecting the coherence between them. The latter is detected by scattering a weak off-resonant probe pulse $E_3(t)$ of frequency ω_3 from the atomic ensemble and detecting the FWM signal $E_4(t)$ at $\omega_4 = \omega_1 + \omega_2 - \omega_3$. Fine structure splitting of states $|5p\rangle$ (into $5p_{1/2}$ and $5p_{3/2}$) and $|4d\rangle$ (into $4d_{3/2}$ and $4d_{5/2}$) has been taken into account in the numerical analysis presented below. To account for additional Stark shifts, we have also considered five far-off-resonant transitions with frequencies falling within 100 nm from the frequencies of both pump pulses. Those transitions are (i) $5p \rightarrow 5d$ at 762 and 776 nm; (ii) $5p \rightarrow 6s$ at 1367 nm; (iii) $4d \rightarrow 4f$ at 1344 nm; (iv) $4d \rightarrow 7f$ at 827 nm; and (v) $4d \rightarrow 8f$ at 793 nm. The two former ones, originating at $|5p\rangle$, have been included in the numerical analysis (Fig. 1), whereas the transitions originating at $|4d\rangle$ have been neglected due to much weaker transition strengths [23].

We first describe the numerical procedure for calculating the four-wave mixing field. Following the standard derivation starting from the wave equation for a lossless dispersionless medium, and using the approximations of a slowly varying field envelope and perfect phase matching [24], one arrives at

$$E_4(t) = -\frac{2\pi i L}{|\mathbf{k}_4|c^2} \frac{\partial^2}{\partial t^2} P^{(3)}(t) \approx \frac{2\pi i L \omega_4^2}{|\mathbf{k}_4|c^2} P^{(3)}(t), \quad (1)$$

where $\mathbf{k}_4 = \mathbf{k}_1 + \mathbf{k}_2 - \mathbf{k}_3$ with \mathbf{k}_n being the wave vector of the corresponding excitation field, L is the interaction length, c is the speed of light, and $P^{(3)}(t)$ is the third-order polarization induced in the medium by the two pump and one probe laser fields. The latter is proportional to the expectation value of the electric dipole moment operator $\hat{\mu}$, which can be derived from the time-dependent density matrix of the atomic ensemble, yielding

$$P^{(3)}(t) = N \langle \hat{\mu} \rangle(t) = N \text{Tr}\{\hat{\rho}(t)\hat{\mu}\}, \quad (2)$$

with N being the number density of atoms. Hereafter, all vector quantities are treated as scalars due to the collinear polarization of the excitation fields.

We calculate $\hat{\rho}(t)$ [and hence $P^{(3)}(t)$] by numerically solving Schrödinger's equation for the wave function $\psi(t)$, which can be expanded in the basis of bare atomic states $|n\rangle$ as

$$\psi(t) = \sum_n a_n(t) e^{-i\omega_n t} |n\rangle. \quad (3)$$

Here, $\hbar\omega_{nm}$ is the energy difference between states $|n\rangle$ and $|m\rangle$. The interaction Hamiltonian has been taken in the usual form of $\hat{V}(t) = -\hat{\mu}E(t)$, where $E(t) = \sum_{k=1}^3 E_k(t)$ represents the total electric field of the three excitation pulses. Seven atomic bare states which have been included in our numerical calculations are shown in Fig. 1, whereas the values of the corresponding matrix elements of the dipole moment have been taken from [23].

In the experimental work presented here and described in detail below, we have recorded the spectrum of the FWM signal as a function of the delay between the pump pulses (both fixed in time and overlapping with one another) and a probe pulse whose time of arrival τ is scanned. A typical sequence of the excitation pulses for a given value of τ is shown in Fig. 2(a).

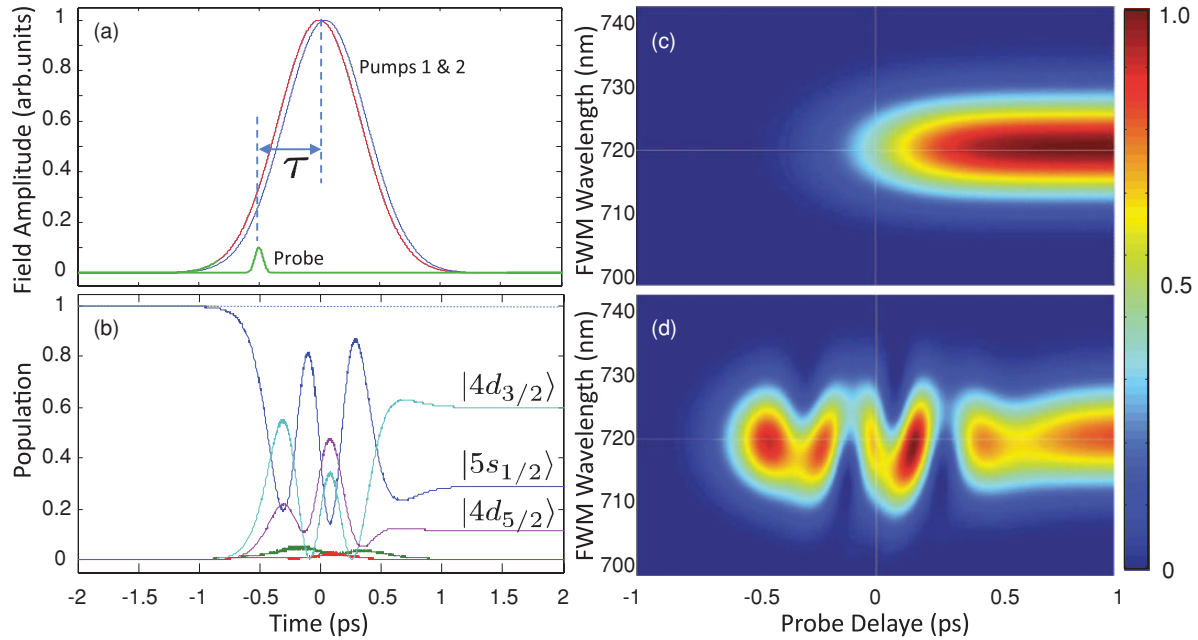


FIG. 2. (Color online) (a) Example of a pulse sequence for a given value of probe delay τ . (b) Example of the numerically calculated populations $|a_n(t)|^2$ [Eq. (3)]. Weak oscillations near zero (green and red) correspond to states $5p_{1/2}$ and $5p_{3/2}$ (not labeled). Examples of the calculated 2D time-frequency “FWM spectrograms” $I_4(\omega_4, \tau)$ are shown for (c) weak- and (d) strong-field excitation.

To calculate the measured signal, we first solve the time-dependent Schrödinger equation for the total excitation field $E(t)$. Complex wave-function amplitudes $a_n(t)$ are calculated as functions of time throughout the excitation pulse sequence. [A typical result for the populations $|a_n(t)|^2$ is shown in Fig. 2(b).] A time-dependent density matrix is then substituted into Eq. (2), and the signal field is calculated according to Eq. (1). The calculation of the observed FWM spectrum $I_4(\omega) = |E_4(\omega)|^2$, with $E_4(\omega)$ being the Fourier transform of $E_4(t)$, has been repeated for each time delay τ . This resulted in a two-dimensional (2D) time-frequency “FWM spectrogram” $I_4(\omega_4, \tau)$. Two examples of this spectrogram for the case of weak- and strong-field excitation are shown in Figs. 2(c) and 2(d), respectively. Note that while the signal is rising uniformly in the weak-field regime [Fig. 2(c)], it oscillates due to Rabi oscillations of the atomic population under the strong-field excitation [Fig. 2(d)], decreasing almost to zero at the moments of substantial transfer of the population back to the ground state [e.g., around 250 fs in Fig. 2(d)].

III. EXPERIMENTAL PROCEDURE AND RESULTS

Experimental FWM spectrograms have been obtained using the setup shown in Fig. 3. The experiments employed a laser system based on a femtosecond Ti:sapphire oscillator (Synergy, Femtolasers), a regenerative amplifier (Spitfire Pro, Spectra Physics), and an optical parametric amplifier (OPA) (Topas, Light Conversion). The amplifier generated 3-mJ, 35-fs pulses at the central wavelength of 800 nm and a 1-kHz repetition rate. In our experiments, these pulses were used as pump 1 (see Fig. 1). A portion of the 800-nm beam (1 mJ) was used to pump an OPA, tuned to the signal and idler wavelengths of 1425 and 1824 nm, which served as pump 2 and probe, respectively. Both pumps 1 and 2 were coupled into home-built

spectral filters consisting of a diffraction grating, a lens, and a plane silver mirror, one focal length apart from one another (Fig. 3). A small tilt of the mirror enabled us to separate the input and output beams in space. A variable slit was installed between the lens and the back mirror to select the necessary

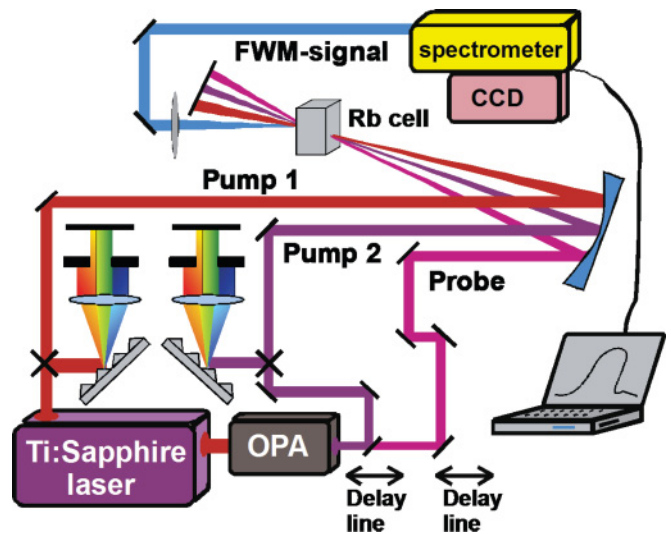


FIG. 3. (Color online) Diagram of the experimental setup. Ti:sapphire regenerative amplifier generates 35-fs, 3-mJ pulses at a 1-kHz repetition rate. Fundamental radiation at 800 nm serves as pump 1. An OPA is used to produce the pump 2 and probe pulses at 1425 and 1824 nm, respectively. Both pumps are spectrally narrowed with home-built spectral filters down to a bandwidth corresponding to ≈ 800 -fs pulse length. All three input pulses are overlapped in BOXCAR geometry and focused into 5-cm optical path Rb cell. A FWM signal is coupled into a spectrometer and detected by a cooled CCD camera.

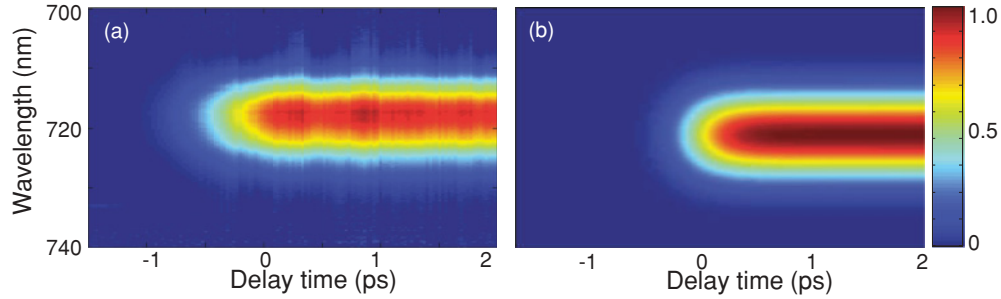


FIG. 4. (Color online) 2D FWM spectrograms for the case of weak-field excitation. (a) Experimental signal detected for the energies of pumps 1 and 2 equal to ≈ 0.2 and $\approx 0.02 \mu\text{J}$, respectively. (b) Numerical simulations with the energies of both pump pulses set to $0.01 \mu\text{J}$. Both spectrograms show signal rising around zero delay time between the scanned probe and fixed overlapping pumps. The observed rise time corresponds to the duration of both pumps (800 fs). The long tail reflects the long relaxation time of the excited $|4d\rangle$ state of Rb.

spectral bandwidth. For both pumps 1 and 2, we cut out about 20 cm^{-1} of bandwidth, corresponding to a pulse duration of about 800 fs. Probe pulses were not spectrally filtered and had a duration of about 80 fs.

All three beams were synchronized in time, collimated, and focused in (BOXCARS) geometry with 25-cm focal distance silver mirror into a 5-cm optical path Rb cell. The temperature of the Rb cell was stabilized at 215°C , which corresponds to a vapor pressure of about 0.05 Torr. The energy of each beam was varied independently with neutral density filters. A FWM signal was spatially separated from the three input beams and coupled into a spectrometer (Model 2035, McPherson), operating with a spectral resolution of 0.5 nm and equipped with a cooled charge-coupled device (CCD) camera (iDus, Andor). The exposure time was set to 0.5 s, and the FWM spectrum was recorded as a function of the probe delay, controlled with a precision translation stage.

To investigate the weak-field regime first, we set the energies of pumps 1 and 2 to ≈ 0.2 and $\approx 0.02 \mu\text{J}$, respectively. A recorded 2D spectrogram [Fig. 4(a)] shows a uniform spectral response with the rising edge corresponding to the pulse duration of pump pulses, and a long tail for the positive delay time reflecting a much longer lifetime of the $|4d\rangle$ state. The spectral width of the signal is equal to that of the probe field. The spectrogram agrees well with the numerically calculated spectrogram shown in Fig. 4(b), and simply shows the two-photon-induced coherence between the unperturbed bare ground and excited states.

When the energy of pump 2 has been increased to the same energy level as pump 1, $\approx 0.1 \mu\text{J}$, the 2D four-wave-mixing spectrogram showed a double-peak structure as seen in Fig. 5(a). This oscillatory behavior is a result of the strong-field modulation of the induced coherence with a two-photon Rabi frequency. As described in the next section, the observed structure reflects the evolution of atomic quantum states during the interaction with the strong pump fields. The oscillations are followed by a long tail similar to the weak-field regime, although now its relative amplitude is very sensitive to the exact energies of pump pulses. A similar double-peak structure has been reproduced in our numerical results shown in Fig. 5(b).

IV. THEORETICAL ANALYSIS

We now turn to the analysis of FWM spectrograms and show their utility in understanding the dynamics of a strongly driven system. We first simplify the interaction picture by reducing it to a three-level model (see inset in Fig. 1). Generalization to an arbitrary number of levels will be discussed later in the text. Let us introduce the following wave functions:

$$\psi^{(k)}(t) = \sum_{n=1}^3 a_n^{(k)}(t) e^{-i\omega_n t} |n\rangle, \quad (4)$$

describing the initial ground state of the system ($k = 0$) and the states of the system interacting with one probe field only ($k = 1$), two strong pump fields ($k = 2$), and all three fields

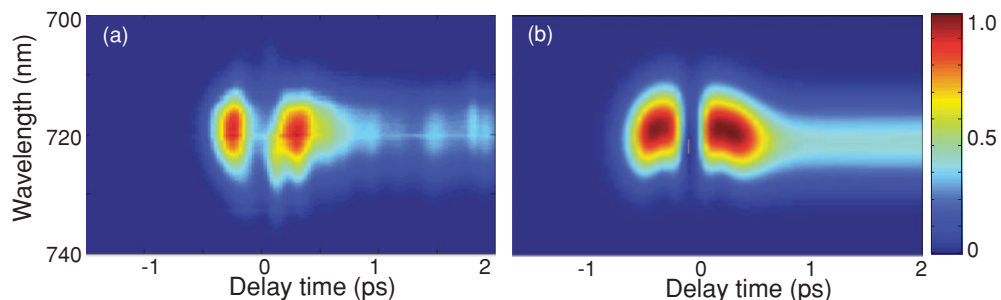


FIG. 5. (Color online) 2D FWM spectrograms for the case of strong-field excitation. (a) Energies of pumps 1 and 2 are ≈ 0.2 and $\approx 0.1 \mu\text{J}$, respectively. (b) Numerical results for the pulse energies of 0.275 and $0.175 \mu\text{J}$. The double-peak structure around time zero represents complicated transient dynamics of the atomic system interacting with two strong pump fields. The long tail at positive delay corresponds to a field-free relaxation of the excited $|4d\rangle$ state of Rb.

together ($k = 3$). Note that hereafter, superscript (k) denotes the number of excitation fields taken into account rather than the expansion order in perturbation theory. For instance, due to the strong-field nature of the interaction, amplitudes $a_n^{(2)}(t)$ in the above expansion of $\psi^{(2)}(t)$ are not necessarily small and linear in $E_{1,2}$. The main contribution to the polarization oscillating at, or close to, the signal frequency ω_4 can be expressed as

$$P^{(3)}(t) = N[\langle \psi^{(0)}(t) | \hat{\mu} | \psi^{(3)}(t) \rangle + \text{c.c.}], \quad (5)$$

where we have neglected the terms proportional to $\langle \psi^{(1)}(t) | \hat{\mu} | \psi^{(2)}(t) \rangle$ because the frequency detuning of the probe field from the lower transition frequency ω_{21} is almost seven times bigger than the corresponding detuning from the upper transition frequency ω_{32} . Substituting Eq. (4) into Eq. (5), one arrives at

$$P^{(3)}(t) = N[\mu_{12} a_1^{(0)*}(t) a_2^{(3)}(t) e^{-i\omega_{21}t} + \text{c.c.}], \quad (6)$$

where μ_{nm} denote matrix elements of the dipole moment. Unlike the effect of strong pump pulses, the effect of a weak probe field E_3 can be treated perturbatively. To the first order in *probe* perturbation [24],

$$a_2^{(3)}(t) = \frac{\mu_{23}}{i\hbar} \int_{-\infty}^t dt' E_3(t') a_3^{(2)}(t') e^{i\omega_{23}t'}. \quad (7)$$

By substituting the above expression into Eq. (6), the response of a three-level atom at frequency ω_4 can be calculated for arbitrarily strong pump fields. Before proceeding to that step, it is instructive to apply this result to the case when all three excitation pulses are weak. In this limit, second-order perturbation theory gives [24]

$$a_3^{(2)}(t') = \frac{\mu_{12}\mu_{23}}{\hbar^2 \Delta_1} \int_{-\infty}^{\infty} d\Omega \frac{E^{(2)}(\Omega)}{\omega_{31} - \Omega - i\Gamma_{31}} e^{i(\omega_{31} - \Omega)t'}, \quad (8)$$

where $E^{(2)}(\Omega)$ is the spectrum of a two-photon pump field $E^{(2)}(t) \equiv E_1(t) \cdot E_2(t)$, Δ_1 is the one-photon detuning shown in Fig. 1, and Γ_{31} is the coherence decay rate. Combining Eqs. (6), (7), and (8), one finds the familiar result for a weak-field four-wave-mixing process with an intermediate resonance [25]:

$$P_{\text{WF}}^{(3)}(t) = R_{\text{WF}}(t) E_3^*(t), \quad (9)$$

where the two-photon response $R_{\text{WF}}(t)$ is given by

$$R_{\text{WF}}(t) = \frac{\mu_{12}^2 \mu_{23}^2}{\hbar^3 \Delta_1 \Delta_3} \int_{-\infty}^{\infty} d\Omega \frac{E^{(2)}(\Omega)}{\omega_{31} - \Omega - i\Gamma_{31}}. \quad (10)$$

In the case of arbitrarily strong pump pulses, Eq. (8) is not applicable and must be replaced by the generic expansion of $a_3^{(2)}(t')$ in spectral components:

$$a_3^{(2)}(t') = \int_{-\infty}^{\infty} d\omega a_3^{(2)}(\omega) e^{-i\omega t'}. \quad (11)$$

This results in the following expression for the third-order polarization in the strong-field regime:

$$P_{\text{SF}}^{(3)}(t) = -\frac{\mu_{12}\mu_{23}}{\hbar} E_3^*(t) e^{-i\omega_{31}t} \int_{-\infty}^{\infty} d\omega \frac{a_3^{(2)}(\omega) e^{-i\omega t}}{\omega_{32} - \omega_3 - \omega}. \quad (12)$$

As confirmed by our numerical and experimental data (Fig. 7), even in the strong-field limit achieved with our experimental

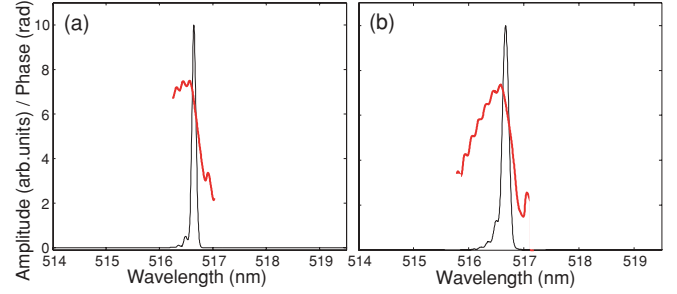


FIG. 6. (Color online) Amplitude (thin black) and phase (thick red) of a *weak-field* atomic response function, retrieved from the (a) experimentally observed and (b) numerically calculated FWM spectrograms. Retrieved spectra show a single resonance corresponding to the $|4d\rangle$ state of rubidium. Its line width is dictated by the spectral resolution of the XFROG method. The spectral phase shows a sharp step across the resonance, typical for a Lorentzian response.

parameters, the spectral width of $a_3^{(2)}(\omega)$ is much smaller than the probe detuning Δ_3 (a few nanometers vs tens of nanometers, respectively). Though not a generic feature of any strong-field interaction scheme, in our particular case, it enables us to simplify the above formula and arrive at the final expression for the strong-field FWM polarization:

$$P_{\text{SF}}^{(3)}(t) \approx \left[-\frac{\mu_{12}\mu_{23}}{\hbar \Delta_3} e^{-i\omega_{31}t} a_3^{(2)}(t) \right] E_3^*(t), \quad (13)$$

which in the case of multiple excited states $|n\rangle$ and $|m\rangle$ can be generalized to

$$P_{\text{SF}}^{(3)}(t) \approx R_{\text{SF}}(t) E_3^*(t), \quad (14)$$

with the response function to the two strong pump fields given by

$$R_{\text{SF}}(t) = -\sum_{nm} \frac{\mu_{1n}\mu_{nm}}{\hbar [\omega_{mn} - \omega_3]} e^{-i\omega_{m1}t} a_m^{(2)}(t). \quad (15)$$

Though not surprising in view of the weak probe approximation, the above result of Eq. (14) means that similarly to the weak-field case of Eq. (9), probe field $E_3(t)$ can be factored out from the third-order polarization of a *strongly driven*

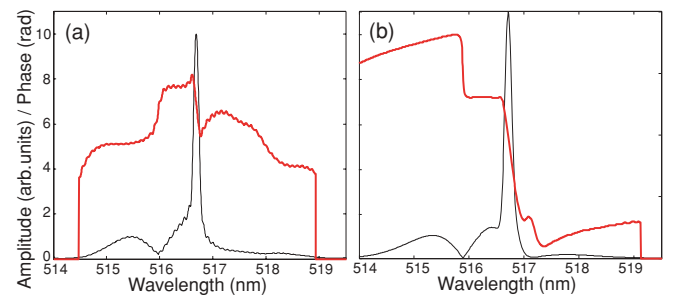


FIG. 7. (Color online) Amplitude (thin black) and phase (thick red) of a *strong-field* atomic response function, retrieved from the (a) experimentally observed and (b) numerically calculated FWM spectrograms [Figs. 5(a) and 5(b), respectively]. The retrieved spectrum shows a narrow resonance, resulting from a field-free decay of $|4d\rangle$, superimposed onto a broad transient response. The latter exhibits clear power broadening and spectral sidebands corresponding to the dynamic Stark splitting under the strong pump excitation.

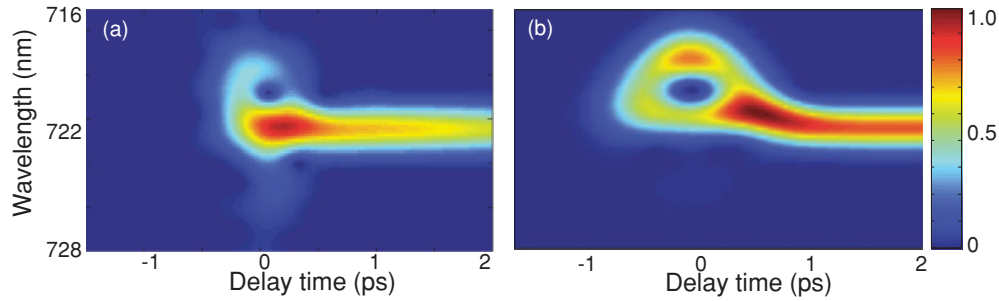


FIG. 8. (Color online) (a) Husimi representation of the experimentally detected atomic response to strong-field excitation, in which spectral resolution has been set to 1.8 nm. (b) Numerically calculated four-wave-mixing spectrogram for a transform limited 500-fs probe pulse (spectral bandwidth of 1.8 nm).

system. However, unlike the perturbative response $R_{WF}(t)$, the strong-field response of Eq. (15) reflects the dynamics of highly oscillatory wave-function amplitudes $a_m^{(2)}(t)$ rather than the frequencies of static atomic resonances appearing in the denominator of Eq. (10). Below, we demonstrate how to retrieve the dynamics of strongly driven atomic states through the analysis of 2D FWM spectrograms.

V. XFROG METHOD

Equation (14) can effectively be viewed as sum-frequency generation between the two fields: that of a probe pulse $E_3(t)$ and the *field* of atomic response $R_{SF}(t)$. The power spectrum of the output “sum-frequency” FWM field $I_4(\omega, \tau) \propto |P^{(3)}(\omega)|^2$ that is recorded as a function of probe delay τ results in 2D four-wave-mixing spectrograms shown in Figs. 4 and 5. The technique of reconstructing an unknown optical field from the spectra of its sum-frequency mixing with a known reference pulse at various time delays has been successfully applied to optical field characterization for many years [26]. This technique, known as cross-correlation frequency resolved optical gating (XFROG), is based on the numerical method of generalized projections [27]. A complete analogy between a conventional optical XFROG trace and a FWM spectrogram enables us to utilize the XFROG algorithm for retrieving an unknown complex-valued atomic response function $R_{SF}(t)$ [Eq. (15)] from the measured spectrogram $I_4(\omega, \tau)$ and precharacterized probe field $E_3(\omega)$. The temporal resolution of the XFROG method is inversely proportional to the spectral

bandwidth of the detected nonlinear signal. The spectral resolution of the method is inversely proportional to the time width of the spectrogram and in our case equals 0.2 nm. The latter dictates the observed line width. For more details on the XFROG approach to coherent nonlinear spectroscopy, see our earlier work on XFROG coherent anti-Stokes Raman scattering (XFROG CARS) [28,29].

We first apply the XFROG method to the weak-field spectrograms shown in Fig. 4. The retrieved response function $R_{WF}(\omega)$ is shown for the case of experimentally [Fig. 6(a)] and numerically [Fig. 6(b)] obtained data. As expected, the retrieved spectrum shows only one peak corresponding to the energy of the unperturbed $|4d\rangle$ state of rubidium — the only quantum state that can be excited with a convoluted bandwidth of pumps 1 and 2 pulses. The spectral resolution of the XFROG method, which is inversely proportional to the temporal width of the spectrogram and in our case equals 0.2 nm, dictates the observed line width. Slow exponential decay, invisible on the time scale of our delay scan, results in a characteristic Lorentzian phase with a phase step across the resonance. Note that the phase is ill defined when the amplitude is zero.

Applying the same retrieval algorithm to the case of a strong-field excitation, e.g., spectrograms shown in Fig. 5, results in a completely different response function. The latter is plotted in Fig. 7. In contrast to the weak-field regime, the spectrum of an atomic response shows a narrow resonance, resulting from a field-free decay of $|4d\rangle$, superimposed onto a power-broadened transient response with clear sidebands corresponding to the energy splitting of the excited state. The magnitude of the splitting and the amplitude ratio of the

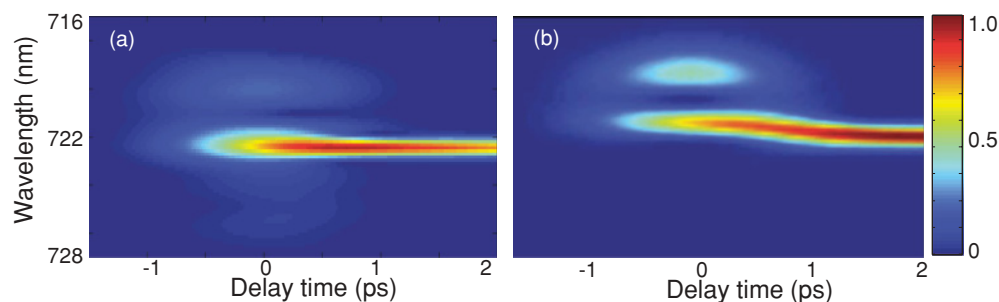


FIG. 9. (Color online) (a) Husimi representation of the experimentally detected atomic response to strong-field excitation, in which spectral resolution has been set to 0.9 nm. (b) Numerically calculated four-wave-mixing spectrogram for a transform limited 1-ps probe pulse (spectral bandwidth of 0.9 nm).

sidebands are very sensitive to the energies of both pump pulses, as well as their length and temporal overlap.

Although the retrieved complex-valued response $R_{SF}(\omega)$ shown in Fig. 7 contains all the information about the dynamics of an atomic wave-function amplitude described by Eq. (15), it is more instructive to analyze these dynamics by inspecting 2D Husimi representations of the same response function, constructed with the desired time and frequency resolution. We note that the ability to represent the dynamics of an atomic system with intuitive Husimi plots is provided by the unique capability of the XFROG technique to retrieve the phase of the complex response function [29]. The 2D Husimi plots shown on the left sides of Figs. 8 and 9 have been calculated by frequency convolving the experimentally retrieved $R_{SF}(\omega)$ with a reference Gaussian probe pulse $E_{ref}(\omega)$ while changing the delay of this pulse in time. Effectively, this procedure is equivalent to measuring the FWM spectrogram with a new probe pulse of variable duration and, hence, bandwidth. Calculated spectrograms are shown on the right sides of Figs. 8 and 9 for comparison.

In Fig. 8(a), we plot the Husimi representation of an atomic response function with the frequency resolution of 1.8 nm. This resolution is higher than that available from the originally detected four-wave-mixing spectrogram (Fig. 5) and corresponds to the duration of the probe pulse of 500 fs. A spectrogram, numerically calculated for the probe pulse of this length, is shown in Fig. 8(b). The two plots are similar and show dynamic splitting of $|4d\rangle$ under strong excitation pump pulses around time zero. Unlike the originally detected spectrogram of Fig. 5, the temporal Rabi oscillations are less obvious, but the spectral splitting is more pronounced. The spectral width of a long tail, corresponding to the field-free relaxation, is determined by the 1.8 nm bandwidth of the chosen probe pulse.

Figure 9 is similar to Fig. 8. Here, the spectral resolution has been further improved from 1.8 to 0.9 nm at the expense of lower resolution in time (from 500 fs to 1 ps). As a result, the temporal oscillations are completely washed out, whereas the dynamic energy splitting is seen more clearly. The latter is

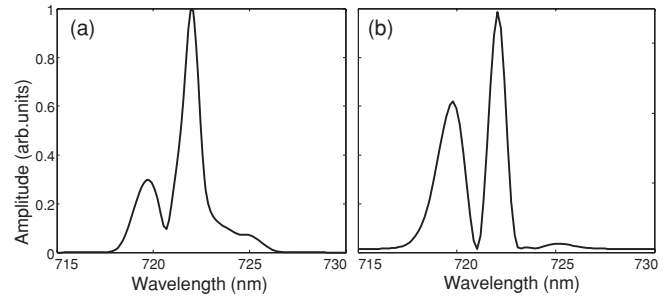


FIG. 10. Vertical cross sections of the 2D plots in Figs. 9(a) and 9(b), respectively, at time zero.

explicitly shown in Fig. 10, where we plot vertical cross sections of the 2D Husimi representation of the atomic strong-field response obtained from the experimental [Fig. 9(a)] and theoretical [Fig. 9(b)] FWM spectrograms.

In summary, we have applied the method of cross-correlation frequency resolved optical gating for mapping out (both in time and frequency) the transient dynamics of an atomic system significantly perturbed by a strong two-photon excitation field. The method is not limited to tracking the dynamics of the atomic population, but is rather capable of reconstructing the full complex amplitude of a quantum state of interest. Using XFROG reconstruction, we have directly observed such effects of a strong-field interaction regime as two-photon Rabi splitting, energy shifting, and power broadening. The technique of an optical gating of the atomic response by means of a parametric scattering process has enabled us to analyze the strong-field effects with variable and easily adjustable resolution in time and frequency.

ACKNOWLEDGMENTS

We would like to thank Xiaoji Xu and Xuan Li for valuable discussions. This work is supported by the CFI, BCKDF, and NSERC.

-
- [1] T. Witte *et al.*, *J. Chem. Phys.* **118**, 2021 (2003).
 - [2] C. Trallero-Herrero and T. C. Weinacht, *Phys. Rev. A* **75**, 063401 (2007).
 - [3] V. Blanchet, C. Nicole, M. A. Bouchene, and B. Girard, *Phys. Rev. Lett.* **78**, 2716 (1997).
 - [4] B. Chatel, J. Degert, S. Stock, and B. Girard, *Phys. Rev. A* **68**, 041402 (2003).
 - [5] M. Wollenhaupt, A. Assion, O. Bazhan, C. Horn, D. Liese, C. Sarpe-Tudoran, M. Winter, and T. Baumert, *Phys. Rev. A* **68**, 015401 (2003).
 - [6] S. Zhdanovich, E. A. Shapiro, M. Shapiro, J. W. Hepburn, and V. Milner, *Phys. Rev. Lett.* **100**, 103004 (2008).
 - [7] R. R. Jones, *Phys. Rev. Lett.* **74**, 1091 (1995).
 - [8] B. Chatel, J. Degert, and B. Girard, *Phys. Rev. A* **70**, 053414 (2004).
 - [9] M. Wollenhaupt *et al.*, *Appl. Phys. B* **82**, 183 (2006).
 - [10] M. Krug *et al.*, *New J. Phys.* **11**, 105051 (2009).
 - [11] M. Wollenhaupt, A. Prakelt, C. Sarpe-Tudoran, D. Liese, T. Bayer, and T. Baumert, *Phys. Rev. A* **73**, 063409 (2006).
 - [12] S. Zhdanovich, E. A. Shapiro, J. W. Hepburn, M. Shapiro, and V. Milner, *Phys. Rev. A* **80**, 63405 (2009).
 - [13] N. Dudovich, T. Polack, A. Peer, and Y. Silberberg, *Phys. Rev. Lett.* **94**, 083002 (2005).
 - [14] T. Bayer, M. Wollenhaupt, C. Sarpe-Tudoran, and T. Baumert, *Phys. Rev. Lett.* **102**, 023004 (2009).
 - [15] F. A. Hashmi and M. A. Bouchene, *Phys. Rev. A* **79**, 025401 (2009).
 - [16] T. Hornung *et al.*, *Appl. Phys. B* **71**, 277 (2000).
 - [17] C. Trallero-Herrero, J. L. Cohen, and T. Weinacht, *Phys. Rev. Lett.* **96**, 063603 (2006).
 - [18] E. A. Shapiro, V. Milner, and M. Shapiro, *Phys. Rev. A* **79**, 023422 (2009).
 - [19] R. R. Jones, *Phys. Rev. Lett.* **75**, 1491 (1995).

- [20] G. Gibson, T. S. Luk, A. McPherson, and C. K. Rhodes, *Phys. Rev. A* **43**, 371 (1991).
- [21] A. S. Zibrov, M. D. Lukin, L. Hollberg, and M. O. Scully, *Phys. Rev. A* **65**, 051801 (2002).
- [22] C. Trallero-Herrero, M. Spanner, and T. Weinacht, *Phys. Rev. A* **74**, 051403 (2006).
- [23] Yu. Ralchenko, A. E. Kramida, J. Reader, and NIST ASD Team, NIST Atomic Spectra Database, ver. 3.1.5 (National Institute of Standards and Technology, Gaithersburg, 2008), [<http://physics.nist.gov/asd3>].
- [24] R. W. Boyd, *Nonlinear Optics*, 2nd ed. (Academic, New York, 2003).
- [25] M. S. Malcuit, D. J. Gauthier, and R. W. Boyd, *Phys. Rev. Lett.* **55**, 1086 (1985).
- [26] S. Linden, H. Giessen, and J. Kuhl, *Phys. Status Solidi B* **206**, 119 (1998).
- [27] K. W. DeLong *et al.*, *Opt. Lett.* **19**, 2152 (1994).
- [28] X. G. Xu *et al.*, *J. Chem. Phys.* **126**, 091102 (2007).
- [29] S. O. Konorov *et al.*, *J. Chem. Phys.* **130**, 234505 (2009).